Monthly Notices
of the
ROYAL ASTRONOMICAL SOCIETY

MNRAS **481,** L79–L83 (2018) doi:10.1093/mnrasl/sly160

Protonated CO_2 in massive star-forming clumps

F. Fontani,[1]★ A. Vagnoli,[2] M. Padovani,[1] L. Colzi,[1,2] P. Caselli[3] and V. M. Rivilla[1]

[1]*INAF-Osservatorio Astrofisico di Arcetri, Largo E. Fermi 5, I-50125 Florence, Italy*
[2]*Dipartimento di Fisica e Astronomia, Università degli Studi di Firenze, I-50125 Florence, Italy*
[3]*Centre for Astrochemical Studies, Max-Planck-Institute for Extraterrestrial Physics, Giessenbachstrasse 1, 85748 Garching, Germany*

Accepted 2018 August 23. Received 2018 August 23; in original form 2018 July 18

ABSTRACT

Interstellar CO_2 is an important reservoir of carbon and oxygen, and one of the major constituents of the icy mantles of dust grains, but it is not observable directly in cold gas because it has no permanent dipole moment. Its protonated form, $HOCO^+$, is believed to be a good proxy for gaseous CO_2. However, it has been detected in only a few star-forming regions to date, so its interstellar chemistry is not well understood. We present new detections of $HOCO^+$ lines in 11 high-mass star-forming clumps. Our observations more than treble the number of detections in star-forming regions to date. We derived beam-averaged abundances relative to H_2 of between 0.3 and 3.8 $\times$ 10^{-11}. We compared these values with the abundances of $H^{13}CO^+$, a possible gas-phase precursor of $HOCO^+$, and of CH_3OH, a product of surface chemistry. We found a positive correlation with $H^{13}CO^+$, but no correlation with CH_3OH. We suggest that the gas-phase formation route starting from HCO^+ plays an important role in the formation of $HOCO^+$, perhaps more important than protonation of CO_2 (upon evaporation of CO_2 from icy dust mantles).

Key words: stars: formation – ISM: clouds – ISM: molecules – radio lines: ISM.

1 INTRODUCTION

Carbon dioxide (CO_2) is an important molecular species in a variety of interstellar environments. In comets, planetary atmospheres and interstellar ices, its abundance is a significant fraction ($\sim$0.1−0.5) of that of water (e.g. Bergin et al. 2005; Whittet et al. 2009; McKay et al. 2016; Hoang et al. 2017). CO_2 ice is one of the main constituents of the icy mantles of dust grains (Öberg et al. 2011). In the gas phase, CO_2 can be observed directly through ro-vibrational transitions (e.g. van Dishoeck et al. 1996), but the lack of a permanent dipole moment, and hence of a pure rotational spectrum, makes it impossible to detect in cold environments. However, its protonated form, $HOCO^+$, has been detected towards the Galactic Centre (Thaddeus, Guelin & Linke 1981; Minh et al. 1991; Neill et al. 2014), in diffuse and translucent clouds (Turner, Terzieva & Herbst 1999) but only in a handful of star-forming regions: in the low-mass pre-stellar core L1544 (Vastel et al. 2016), in the protostars L1527 and IRAS 16293–2422 (Sakai et al. 2008; Majumdar et al. 2018) and in the protostellar shock L1157–B1 (Podio et al. 2014).

For a cold and dense gas, two main chemical formation pathways have been proposed: (1) a gas-phase route from the reaction $HCO^+ + OH \leftrightarrow HOCO^+ + H$, and (2) the protonation of CO_2 (mainly upon reaction with H_3^+) desorbed from grain mantles (see e.g. Bizzocchi et al. 2016; Vastel et al. 2016). In scenario (1), CO_2 would be a product of $HOCO^+$ (after dissociative recombination), while the opposite is expected in scenario (2). Owing to the lack of stringent observational constraints, it is currently unclear which of these two mechanisms is dominant, and under which physical conditions they occur. Constraining the abundance of $HOCO^+$ has important implications also for the abundance of CO_2 in ice. In fact, if $HOCO^+$ is formed in a cold gas and then, upon dissociative recombination, gives rise to CO_2, the resulting CO_2could freeze-out on grain mantles and contribute to the amount of CO_2 ice observed in dark clouds (Bergin et al. 2005), although this cannot explain the large amount of solid CO_2 measured along the line of sight of background stars (Boogert, Gerakines & Whittet 2015) or in deeply embedded massive young stars (van Dishoeck et al. 1996). In fact, the formation of CO_2 ice from surface reactions is still debated. Laboratory experiments have suggested that CO_2 ice forms from $CO + O \rightarrow CO_2$ (D'Hendecourt et al. 1986), but this reaction requires strong UV irradiation, and hence it is expected to be inefficient in dark clouds. Other surface reactions have been proposed, such as cosmic-ray bombardment on carbonaceous grains covered by water ice (Mennella, Palumbo & Baratta 2004), or the radical–radical reaction $OH + CO \rightarrow CO_2 + H$ (Garrod & Pauly 2011; Ioppolo et al. 2011; Noble et al. 2011). This latter process involves the diffusion of heavy radicals, however, which is difficult at dust temperatures below $\sim$30 K. Although high-precision measurements are not currently available, new promising techniques have been proposed (e.g. Cooke, Fayolle & Öberg 2016) that will shed light on this important surface chemistry process.

In this paper, we present new detections of $HOCO^+$ in 11 high-mass star-forming regions, which belong to an evolutionary sample

★ E-mail: fontani@arcetri.astro.it

of 27 clumps divided into the three main evolutionary categories of the massive-star formation process (Fontani et al. 2011): high-mass starless cores (HMSCs), high-mass protostellar objects (HMPOs) and ultra-compact H II regions (UCHIIs). The sample has been extensively observed in several dense gas tracers, with the aim of studying the chemical evolution of these molecules during the massive-star formation process (Fontani et al. 2011, 2014, 2015a,b, 2016; Colzi et al. 2018a,b; Mininni et al. 2018). This work represents the first study of protonated carbon dioxide in a statistically relevant number of star-forming regions.

2 OBSERVATIONS

The spectra analysed in this work are part of the data set presented in Colzi et al. (2018a). These data were obtained with the IRAM 30-m telescope in the 3-mm band with the EMIR receiver, covering the frequency ranges 85.31–87.13 and 88.59–90.41 GHz, towards 26 dense cores in massive-star-forming regions divided into the three evolutionary categories HMSCs, HMPOs and UCHIIs (see Section 1). For details on the source selection, see Fontani et al. (2011). The atmospheric conditions were very stable, with amounts of precipitable water vapour in the range 3–8 mm. We observed in wobbler-switching mode (wobbler throw of 240 arcsec). Pointing was checked almost every hour on nearby quasars, planets, or bright H II regions. The data were calibrated with the chopper wheel technique (see Kutner & Ulich 1981), and the calibration uncertainty was estimated to be about 10 per cent. More details are given in Colzi et al. (2018a). The spectra were reduced and analysed with the software CLASS of the GILDAS package. The detected lines were fitted with a Gaussian shape.

3 RESULTS

Table 1 lists the 27 observed sources: 11 HMSCs, 9 HMPOs and 7 UCHIIs. We detected clearly (signal-to-noise ratio $\geq$5) the $HOCO^+$ $4_{0,4} - 3_{0,3}$ transition ($HOCO^+$ 4–3 hereafter, $E_{up} \sim 10.3$ K) at 85531.497 MHz (Bizzocchi et al. 2016) in five HMSCs, two HMPOs and four UCHIIs. The spectra of the detected sources are shown in Fig. 1. The relatively high detection ($\sim$50 per cent) in the HMSCs indicates that $HOCO^+$ is a species that is abundant in cold and dense gas. The detection rate decreases during the HMPO phase ($\sim$22 per cent), and then it increases again in the UCHII stage ($\sim$57 per cent). Because we detected only one transition of $HOCO^+$, in order to confirm that the detected line is indeed $HOCO^+$ and rule out contamination by transitions of other molecules we simulated the spectrum of one of the two sources in which the line has the highest intensity peak, namely 05358–mm1 (Fig. 1), and used the software MADCUBA[1] to search for the emission of nearby lines potentially blended with $HOCO^+$ 4–3. Belloche et al. (2013) showed that in Sgr B2(N) the only species with lines that could contaminate $HOCO^+$ 4–3 is C_2H_3CN. They found C_2H_3CN column densities above 10^{18} cm^{-2} and line widths larger than those that we found for $HOCO^+$. In order to simulate the spectrum, we assumed for the excitation temperature the kinetic temperature obtained from ammonia (39 K, Fontani et al. 2011) and the same line width as obtained from fitting $HOCO^+$ 4–3 (4.9 km s^{-1}). As shown in Fig. 2 (top panel), even assuming a very high column density of 10^{18} cm^{-2} as in Sgr B2(N), the expected C_2H_3CN line intensities are well below the spectral rms, and well separated from the $HOCO^+$ 4–3 line. Another transition of $HOCO^+$, namely the $4_{1,3} - 3_{1,2}$ line centred at 85852.8576 MHz ($E_u \sim 48$ K), falls in our band but is undetected. Because its line strength and Einstein coefficient are quite similar to those of the $4_{0,4} - 3_{0,3}$ transition (see Bizzocchi et al. 2016), we investigated whether its non-detection is caused by a lack of sensitivity. Fig. 2 (bottom panel) shows that the synthetic spectrum of 05358–mm1 around this line (simulated assuming the parameters described above for $HOCO^+$) is indeed consistent with a non-detection. Because this source shows the highest intensity peak of $HOCO^+$ 4–3, we can reasonably conclude that the non-detection of the second transition is caused by a sensitivity limit in all sources.

All detected lines are well fitted by a single Gaussian (Fig. 1). The results of the fit performed as explained in Section 2, namely the line-integrated intensity ($\int T_{MB} dv$), the peak velocity in the LSR (v_p), and the line width at half-maximum (Δv), are shown in Table 1. The uncertainties on $\int T_{MB} dv$ are calculated from the expression $\sigma \Delta v_{res} \sqrt{n}$, obtained from the propagation of errors, where σ is the 1σ rms noise in the spectrum, Δv_{res} is the spectral resolution, and n is the number of channels with signal. The uncertainties on v_p and Δv are computed by the fit procedure. The Δv measured towards the detected UCHII regions are always larger than $\sim$3.2 km s^{-1}, while they are narrower than 3 km s^{-1} in all HMSCs (but in 05358–mm3), in agreement with the fact that the envelopes of UCHII regions are more turbulent than those of HMSCs. The case of 05358–mm3 is peculiar because this core is probably externally heated (Fontani et al. 2011), and hence its chemical composition and the emission that we observe is probably a mix between the cold and dense core nucleus and the warmer envelope. The line shapes are symmetric and do not show non-Gaussian wings. This suggests that in all sources the $HOCO^+$ emission is associated with the bulk gas. This suggestion is supported by the fact that the peak velocities are consistent with the systemic velocities (given in Fontani et al. 2011) within the uncertainties (see Fig. 1).

3.1 $HOCO^+$ column densities and fractional abundances

From the line-integrated intensity, we calculated the total column density of $HOCO^+$ assuming local thermodynamic equilibrium (LTE) and optically thin conditions from the equation

$$N = \frac{8\pi\nu_{ij}^3}{c^3 A_{ij}} \frac{\int T_{MB} dv}{g_i [J_\nu(T_{ex}) - J_\nu(T_{BG})]} \frac{Q(T_{ex}) \exp(E_j/kT_{ex})}{1 - \exp(-h\nu_{ij}/kT_{ex})}, \quad (1)$$

where ν_{ij} is the frequency of the transition, $A_{ij}$is the Einstein coefficient of spontaneous emission, $g_i$is the statistical weight of the upper level, $E_j$is the energy of the lower level, c is the speed of light, h and k are the Planck and Boltzmann constants, respectively, T_{ex} is the excitation temperature, $Q(T_{ex})$ is the partition function computed at temperature T_{ex}, T_{BG} is the background temperature (assumed to be that of the cosmic microwave background, 2.7 K), and $J_\nu(T)$ is the equivalent Rayleigh–Jeans temperature (see also equation A4 in Caselli et al. 2002). The line strength, energy of the upper level, and Einstein coefficient of spontaneous emission are taken from the Cologne Database for Molecular Spectroscopy (CDMS,[2] see also Bogey, Demuynck & Destombes 1986; Bizzocchi et al. 2016), and are $S\mu^2 \sim 29.2$ D^2, $E_u \sim 10.3$ K and $A_{ij} \sim 2.36 \times 10^{-5}$ s^{-1}, respectively. The assumption of optically thin emission is consistent with the low abundance of the molecule and with line shapes without

[1] Madrid Data Cube Analysis on image is a software to visualize and analyse astronomical single spectra and datacubes (Martín et al., in prep.; Rivilla et al. 2016).

[2] https://www.astro.uni-koeln.de/cdms

Table 1. Results derived from Gaussian fits to the lines. In columns 2–6 we give: the integrated intensity ($\int T_{\rm MB}{\rm d}v$), the velocity in the local standard of rest (LSR) at line peak ($v_{\rm p}$), the full width at half-maximum (Δv), the assumed gas excitation temperature ($T_{\rm ex}$), and the HOCO$^+$ beam-averaged total column density, N(HOCO$^+$), calculated as explained in Section 3.1. The uncertainities on N are obtained by propagating the error on $\int T_{\rm MB}{\rm d}v$, to which we sum a 10% of calibration error on the $T_{\rm MB}$ scale (see Section 2) not included in the error on $\int T_{\rm MB}{\rm d}v$. $T_{\rm ex}$ is assumed without uncertainty. Columns 7 and 8 give the submillimetre flux densities, $F_{\rm submm}$, and the H_2 column densities, $N(H_2)$, derived from it, respectively (see Section 3.1 for details). The error on $N(H_2)$ is obtained by propagating the error on $F_{\rm submm}$, to which we add a calibration error of 20% on the SCUBA absolute flux scale at 850 μm (Di Francesco et al. 2008). The HOCO$^+$ fractional abundances, X[HOCO$^+$], are shown in column 9. Finally, in columns 10, 11 and 12, we list the fractional abundances of CH_3OH, $H^{13}CO^+$ and N_2H^+ averaged over 28 arcsec.

Source	$\int T_{\rm MB}{\rm d}v$ [K km s^{-1}]	$v_{\rm p}$ [km s^{-1}]	Δv [km s^{-1}]	$T_{\rm ex}$ [K]	N(HOCO$^+$) [$\times 10^{11}$ cm^{-2}]	$F_{\rm submm}$ [Jy]	$N(H_2)$ [$\times 10^{22}$ cm^{-2}]	X[HOCO$^+$] [$\times 10^{-11}$]	X[CH_3OH] [$\times 10^{-10}$]	X[$H^{13}CO^+$] [$\times 10^{-11}$]	X[N_2H^+] [$\times 10^{-9}$]
					HMSCs						
00117–MM2	≤0.069	–	–	14	≤3	–$^{(u)}$	–	–	–	–	–
AFGL5142–EC$^{(w)}$	0.17 ± 0.03	−1.6 ± 0.3	2.9 ± 0.6	25	9 ± 2	5.1 ± 0.5$^{(s)}$	11.3 ± 3.4	0.8 ± 0.4	28 ± 8	7.4 ± 3.1	2.5 ± 1.4
05358–mm3$^{(w)}$	0.41 ± 0.05	−16.8 ± 0.3	4.8 ± 0.6	30	23 ± 5	6.1 ± 0.2$^{(s)}$	10.6 ± 2.4	2.2 ± 1.0	12 ± 3	–	0.6 ± 0.2
G034–G2	0.08 ± 0.02	41.8 ± 0.2	1.7 ± 0.5	20	4 ± 1	0.88 ± 0.04$^{(a)}$	4.1 ± 1.0	0.9 ± 0.5	2.2 ± 0.5	2.0 ± 0.8	1.5 ± 0.4
G034–F2	≤0.081	–	–	20	≤4	0.36 ± 0.02$^{(s)}$	1.6 ± 0.4	≤2.5	3.1 ± 0.8	1.1 ± 0.4	1.0 ± 0.3
G034–F1	0.04 ± 0.01	58.1 ± 0.2	1.2 ± 0.4	20	1.9 ± 0.4	0.27 ± 0.02$^{(s)}$	1.2 ± 0.3	1.6 ± 1.0	9.8 ± 2.5	6.7 ± 2.7	3.4 ± 1.1
G028–C1	0.14 ± 0.02	79.3 ± 0.2	2.6 ± 0.4	17	6 ± 1	0.93 ± 0.03$^{(s)}$	3.6 ± 0.8	1.7 ± 0.8	3.8 ± 0.9	6 ± 2	2.3 ± 0.6
G028–C3	≤0.084	–	–	17	≤4	0.56 ± 0.03$^{(a)}$	2.4 ± 0.6	≤3.5	–	–	–
I20293–WC	≤0.074	–	–	17	≤3	1.9 ± 0.1$^{(s)}$	7.4 ± 1.9	≤0.4	2.4 ± 0.6	4.9 ± 1.9	1.5 ± 0.5
22134–G$^{(w)}$	≤0.076	–	–	25	≤4	1.6 ± 0.1$^{(s)}$	3.6 ± 0.9	≤1.1	4 ± 1	8.7 ± 3.3	0.4 ± 0.1
22134–B	≤0.071	–	–	17	≤3	0.52 ± 0.05$^{(s)}$	2.0 ± 0.6	≤1.6	0.9 ± 0.3	4.8 ± 2.0	0.9 ± 0.4
					HMPOs						
00117–MM1	≤0.11	–	–	20	≤5	–$^{(u)}$	–	–	–	–	–
AFGL5142–MM	0.15 ± 0.03	−2.5 ± 0.2	2.4 ± 0.4	34	9 ± 3	6.8 ± 0.3$^{(s)}$	10.1 ± 2.4	0.9 ± 0.5	53 ± 13	10 ± 4	2.4 ± 0.7
05358–mm1	0.37 ± 0.04	−17.0 ± 0.2	4.9 ± 0.5	39	25 ± 5	6.1 ± 0.3$^{(s)}$	8.4 ± 2.1	3.0 ± 1.4	30 ± 8	1.0 ± 0.4	1.4 ± 0.04
18089–1732	≤0.13	–	–	38	≤8	7.5 ± 0.4$^{(s)}$	9.6 ± 2.4	≤0.8	67 ± 17	14 ± 5	2.2 ± 0.8
18517+0437	≤0.12	–	–	40	≤8	6.7 ± 0.4$^{(a)}$	7.9 ± 1.3	≤1.0	54 ± 9	21 ± 6	1.1 ± 0.2
G75–core	≤0.10	–	–	96	≤14	10.0 ± 0.4$^{(s)}$	4.4 ± 1.1	≤3.2	69 ± 17	38 ± 14	1.0 ± 0.3
I20293–MM1	≤0.10	–	–	37	≤7	3.7 ± 0.2$^{(s)}$	4.9 ± 1.2	≤1.3	11 ± 3	13 ± 5	9 ± 2
I21307	≤0.087	–	–	21	≤4	1.03 ± 0.04$^{(s)}$	2.9 ± 0.7	≤1.4	4.5 ± 1.1	3.2 ± 1.1	0.8 ± 0.3
I23385	≤0.096	–	–	37	≤6	1.81 ± 0.05$^{(s)}$	2.4 ± 0.6	≤2.6	15 ± 4	9.3 ± 3.3	0.6 ± 0.2
					UCHIIs						
G5.89–0.39	0.26 ± 0.03	9.5 ± 0.2	4.3 ± 0.6	31	15 ± 3	18 ± 1$^{(s)}$	55 ± 14	0.3 ± 0.1	8.5 ± 2	4.2 ± 1.7	0.5 ± 0.1
I19035–VLA1	0.20 ± 0.03	33.3 ± 0.4	6.4 ± 0.9	39	14 ± 3	2.9 ± 0.1$^{(s)}$	3.6 ± 0.9	3.8 ± 1.9	17 ± 4	15 ± 5	5.0 ± 1.5
19410+2336	≤0.15	–	–	21	≤7	4.8 ± 0.1$^{(a)}$	13.6 ± 3.0	≤0.5	5.4 ± 1.2	3.6 ± 1.2	3.2 ± 1.0
ON1	0.20 ± 0.02	11.2 ± 0.2	3.8 ± 0.5	26	10 ± 2	–$^{(u)}$	–	–	–	–	–
I22134–VLA1	≤0.11	–	–	47	≤9	2.1 ± 0.1$^{(s)}$	2.1 ± 0.5	≤4.2	2.9 ± 0.7	2.0 ± 0.7	0.9 ± 0.3
23033+5951	0.12 ± 0.02	−52.4 ± 0.3	3.2 ± 0.5	25	7 ± 2	3.5 ± 0.1$^{(s)}$	7.8 ± 1.8	0.8 ± 0.4	5.7 ± 1.3	9.2 ± 3.1	2.6 ± 1.4
NGC 7538–IRS9	≤0.16	–	–	31	≤10	3.9 ± 0.1$^{(s)}$	11.9 ± 2.7	≤0.8	5.4 ± 1.2	4.1 ± 1.4	0.5 ± 0.1

Notes: $^{(w)}$ 'warm' core having a kinetic temperature higher than 20 K, and probably externally heated (Fontani et al. 2011);
$^{(s)}$ measured from the maps of the SCUBA survey (Di Francesco et al. 2008);
$^{(a)}$ measured from the maps of the APEX ATLASGAL survey (http://www3.mpifr-bonn.mpg.de/div/atlasgal/index.html);
$^{(u)}$ continuum map not available either in the survey of Di Francesco et al. (2008) or in the ATLASGAL survey.

hints of high optical depths (such as, for example, asymmetric or flat-topped profiles). The beam-averaged column densities are in the range $\sim 3.5 \times 10^{11} - 4.6 \times 10^{12}$ cm^{-2}. For undetected lines, we computed the upper limits on $\int T_{\rm MB}{\rm d}v$ assuming a Gaussian line with intensity peak equal to the 3σ rms in the spectrum, and Δv equal to the average value of each evolutionary group, and from this we derived the upper limits on N(HOCO$^+$) from equation (1).

We computed the HOCO$^+$ fractional abundances, X[HOCO$^+$], by dividing the HOCO$^+$ total column densities by those of H_2, $N(H_2)$, derived from the submillimetre continuum emission. This latter was computed from the (sub-)millimetre dust thermal continuum emission extracted from the images of the 850-μm survey of Di Francesco et al. (2008) obtained with SCUBA at the James Clerk Maxwell Telescope (JCMT). We used equation (A1) in Mininni et al. (2018) to compute $N(H_2)$, which assumes optically thin emission, and a gas-to-dust ratio of 100. The submillimetre continuum fluxes, $F_{\rm submm}$, used to compute $N(H_2)$ were extracted from a circular area equivalent to the IRAM 30-m half-power beam width (HPBW) at the frequency of the HOCO$^+$ line, namely ∼28 arcsec. The uncertainty on $F_{\rm submm}$ was calculated from the propagation of errors. The submillimetre fluxes, and the derived $N(H_2)$ and X[HOCO$^+$] obtained as explained above, are given in Table 1. For the sources not present in the survey of Di Francesco et al. (2008), we estimated $N(H_2)$ following the same analysis from the APEX ATLASGAL continuum images (http://www3.mpifr-bonn.mpg.de/div/atlasgal/index.html) at ∼870 GHz. We derive X[HOCO$^+$] in the range 0.3–3.8 $\times$ 10^{-11}. These values are intermediate between those obtained towards the pre-stellar core L1544 (∼5 $\times$ 10^{-11}, Vastel et al. 2016) and towards the hot corino IRAS 16293–2422 (∼1 $\times$ 10^{-13}, Majumdar et al. 2018).

4 DISCUSSION AND CONCLUSIONS

As discussed in Section 1, two main pathways have been proposed for the formation of HOCO$^+$ in dense gas: either the gas-phase reaction HCO$^+$ + OH↔HOCO$^+$ + H or the protonation of desorbed CO_2, mainly upon reaction with H_3^+ (Vastel et al. 2016; Bizzoc-

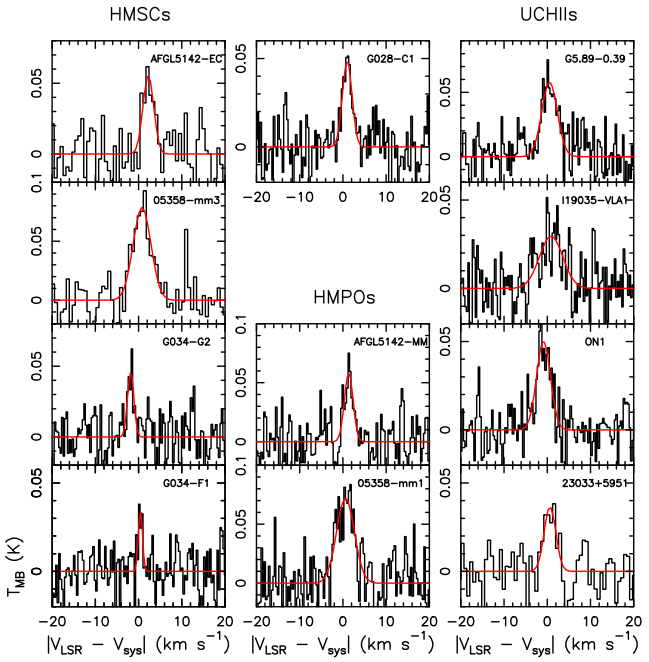

Figure 1. Spectra of the $HOCO^+$ ($4_{0,4} - 3_{0,3}$) line in the 11 detected sources. The *y*-axis is in T_{MB} units. The *x*-axis corresponds to $|V_{LSR} - V_{sys}|$, namely the difference between the local standard of rest velocity, V_{LSR}, and the nominal systemic velocity, V_{sys}, given in Fontani et al. (2011). The red curves superimposed on the spectra represent the best Gaussian fits.

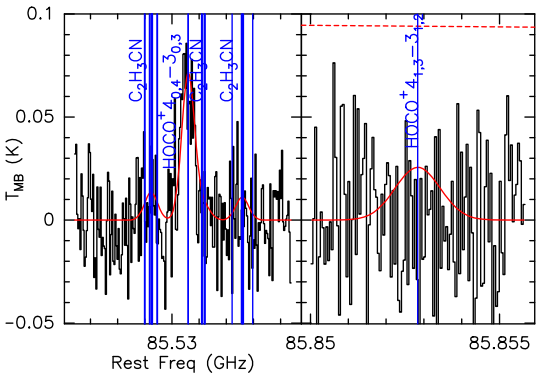

Figure 2. (Left) Spectrum of the $HOCO^+$ $4_{0,4} - 3_{0,3}$ line towards 05358–mm1 superimposed on the synthetic spectrum (in red) calculated with MADCUBA. The synthetic spectrum is calculated for a $HOCO^+$ column density of 4.3×10^{12} cm^{-2} and a C_2H_3CN column density of 10^{18} cm^{-2}, which is the value measured towards Sgr B2(N) (see Section 3). The rest frequencies of the nearby C_2H_3CN transitions are indicated by vertical lines. (Right) Spectrum of 05358–mm1 centred on the rest frequency of $HOCO^+$ $4_{1,3} - 3_{1,2}$, superimposed on the synthetic spectrum created with the same parameters as used in the left-hand panel: the expected peak of the line is well under the 3σ rms noise (shown by the red dashed horizontal line).

chi et al. 2016). To investigate if and how our observational results can put constraints on these alternative pathways, in Fig. 3 we show the fractional abundance of $HOCO^+$ (calculated as explained in Section 3.1) against that of $H^{13}CO^+$, the main precusor of $HOCO^+$ in the gas phase, and that of CH_3OH, a tracer of surface chemistry. For completeness, we also plot X[$HOCO^+$] against X[N_2H^+], because protonation of CO_2 may occur also via reaction with N_2H^+. The CH_3OH and N_2H^+ column densities used to compute X[CH_3OH] and X[N_2H^+] were taken from Fontani et al.

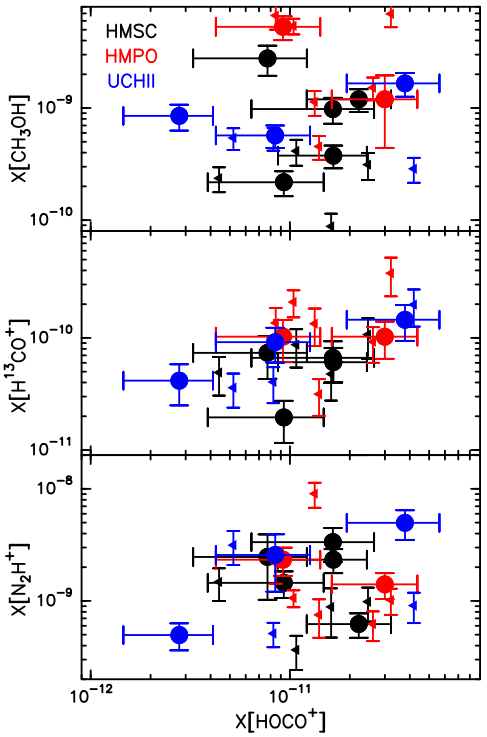

Figure 3. Abundance of $HOCO^+$ against that of, from top to bottom, CH_3OH, $H^{13}CO^+$ and N_2H^+. The colours indicate the different evolutionary groups as labelled in the top-left corner. The large filled symbols correspond to the detected sources, while the small triangles indicate the upper limits on the abundance of $HOCO^+$. In the panel with X[$H^{13}CO^+$], we do not show 05358–mm3, observed and detected in CH_3OH, N_2H^+ and $HOCO^+$ but not in $H^{13}CO^+$.

(2015a) and Fontani et al. (2015b), respectively, and rescaled to the beam of the $HOCO^+$ observations. The $H^{13}CO^+$ column densities used to derive X[$H^{13}CO^+$] were estimated from the integrated intensities of the $H^{13}CO^+$ 1–0 lines at 86754.288 MHz, serendipitously detected in the same data set as described in Section 2 and in Colzi et al. (2018a). We have followed the same approach as used for $HOCO^+$; that is, we assumed optically thin lines and LTE conditions (see Section 3.1). We used the excitation temperatures listed in Table 1. The beam size is almost the same as that of $HOCO^+$, and hence all the fractional abundances in Table 1 are averaged over the same angular region.

Fig. 3 indicates a clear non-correlation between the abundances of CH_3OH and $HOCO^+$, while $H^{13}CO^+$ and $HOCO^+$ seem positively correlated. By applying simple statistical tests to the detected sources only, the correlation coefficient (Pearson's ρ) between X[$HOCO^+$] and X[$H^{13}CO^+$] is 0.7. Considering also the upper limits, the correlation remains positive (Pearson's ρ=0.6). The correlation between X[$HOCO^+$] and X[N_2H^+] is positive (Pearson's ρ=0.4 without the upper limits) but much less convincing. If we assume that both CO_2 and CH_3OH form on grain mantles, and what we find in the gas is evaporated at about the same time, the lack of correlation between X[$HOCO^+$] and both X[CH_3OH] and X[N_2H^+] would indicate that $HOCO^+$ probably does not originate in CO_2 that has evaporated from ice mantles. This interpretation has two significant caveats. First, the formation processes of CO_2 and CH_3OH on the surfaces of dust grains can be different. In fact, CO_2 is thought to form in water-ice mantles of cold carbonaceous grains via cosmic-ray bombardment (Mennella et al. 2004), or via the surface reaction

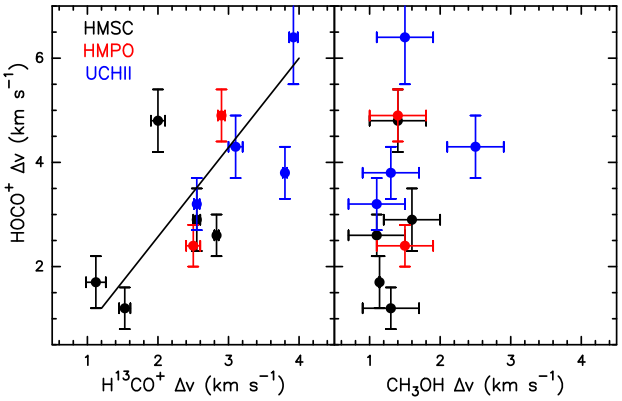

Figure 4. Line widths at half-maximum, Δv, of $H^{13}CO^+$ (left panel) and CH_3OH (right panel) against those of $HOCO^+$. The colours indicate the different evolutionary groups as in Fig. 3. The solid line in the left panel corresponds to a linear fit to the data.

CO + OH at dust temperatures of ∼30 K (Garrod & Pauly 2011), while CH_3OH is formed from the hydrogenation of CO at dust temperatures of ∼10 K (Vasyunin et al. 2017). Second, the main molecular ion responsible for the protonation of CO_2 is H_3^+ and not N_2H^+. Nevertheless, the positive correlation between $X[H^{13}CO^+]$ and $X[HOCO^+]$ suggests a non-negligible, or even dominant, contribution from HCO^+ to the formation of the detected $HOCO^+$. This interpretation of our results is in agreement with the study of Majumdar et al. (2018), who proposed that the dominant (up to 85 per cent) formation route of $HOCO^+$ in the extended and cold ($T \leq 30$ K) envelope of the hot corino IRAS 16293–2422 is indeed from the gas-phase reaction $OH + HCO^+$. The fact that $HOCO^+$ and $H^{13}CO^+$ probably arise from gas with similar physical properties can be understood also from a comparison of their line widths at half-maximum. Fig. 4 indicates that the $HOCO^+$ line widths are correlated with those of $H^{13}CO^+$, but not with those of CH_3OH (which are always narrower). Hence, CH_3OH is probably not associated with the same gas.

Overall, our findings suggest a significant (perhaps dominant) role of HCO^+ as a gas-phase progenitor of $HOCO^+$. However, caution needs to be exercised in the interpretation of our results for two reasons. The first reason is that the $HOCO^+$ column densities, and hence the fractional abundances, were derived assuming an excitation temperature that could not be that of the molecule. To solve this problem, detection of more lines tracing different excitation conditions are required. The second reason arises from the fact that our column densities are values averaged over large (28 arcsec) angular surfaces. Our targets are known to have a complex structure, and temperature (and density) gradients. Therefore, higher-angular-resolution observations are needed to determine the $HOCO^+$-emitting region precisely, and, from this, to gain the understanding of its temperatures and densities that is required to model the chemistry correctly.

ACKNOWLEDGEMENTS

We thank the IRAM 30-m staff for precious help during the observations. We thank the anonymous referee for his/her constructive comments. VMR and MP acknowledge the financial support received from the European Union's Horizon 2020 research and innovation program under the Marie Sklodowska-Curie grant agreement No 664931. LC acknowledges support from the Italian Ministero dell'Istruzione, Università e Ricerca through the grant Progetti Premiali 2012 - iALMA (CUP C52I13000140001). PC acknowledges support from the European Research Council (ERC project PALs 320620).

REFERENCES

Belloche A., Müller H. S. P., Menten K. M., Schilke P., Comito C., 2013, A&A, 559, A47
Bergin E. A., Melnick G. J., Gerakines P. A., Neufeld D. A., Whittet D. C. B., 2005, ApJ, 627, L33
Bizzocchi L., et al., 2017, A&A, 602, A34
Bogey M., Demuynck C., Destombes J.-L., 1986, J. Chem. Phys., 84, 10
Boogert A. C. A., Gerakines P. A., Whittet D. C. B., 2015, ARA&A, 53, 541
Caselli P., Walmsley C. M., Zucconi A., Tafalla M., Dore L., Myers P. C., 2002, ApJ, 565, 344
Colzi L., Fontani F., Caselli P., Ceccarelli C., Hily-Blant P., Bizzocchi L., 2018a, A&A, 609, A129
Colzi L., Fontani F., Rivilla V. M., Sánchez-Monge A., Testi L., Beltrán M. T., Caselli P., 2018b, MNRAS, 478, 3693
Cooke I. R., Fayolle E. C., Öberg K. I., 2016, ApJ, 832, 5
D'Hendecourt L. B., Allamandola L. J., Grim R. J. A., Greenberg J. M., 1986, A&A, 158, 119
Di Francesco J., Johnstone D. Kirk H., MacKenzie T., Ledwosinska E., 2008, ApJS, 175, 277
Fontani F., Palau A., Caselli P., Sánchez-Monge Á., Butler M. J., 2011, A&A, 529, L7
Fontani F., Sakai T., Furuya K., Sakai N., Aikawa Y., Yamamoto S., 2014, MNRAS, 440, 448
Fontani F., Busquet G., Palau A., Caselli P., Sánchez-Monge Á., Tan J. C., Audard M., 2015a, A&A, 575, A87
Fontani F., Caselli P., Palau A., Bizzocchi L., Ceccarelli C., 2015b, ApJ, 808, L46
Fontani F., Rivilla V. M., Caselli P., Vasyunin A., Palau A., 2016, ApJ, 822, L30
Garrod R. T., Pauly T., 2011, ApJ, 735, 15
Hoang M., et al., 2017, A&A, 600, A77
Ioppolo S., van Boheemen Y., Cuppen H. M., van Dishoeck E. F., Linnartz H., 2011, MNRAS, 413, 2281
Kutner M. L., Ulich B. L., 1981, ApJ, 250, 341
Majumdar L., Gratier P., Wakelam V., Caux E., Willacy K., Ressler M. E., 2018, MNRAS, 477, 525
McKay A. J., Kelley M. S. P., Cochran A. L., Bodewits D., DiSanti M. A., Russo N. D., Lisse C. M., 2016, Icarus, 266, 249
Mennella V., Palumbo M. E., Baratta G. A., 2004, ApJ, 615, 1073
Minh Y. C., Brewer M. K., Irvine W. M., Friberg P., Johansson L. E. B., 1991, A&A, 244, 470
Mininni C., Fontani F., Rivilla V. M., Beltrán M. T., Caselli P., Vasyunin A., 2018, MNRAS, 476, L39
Neill J. L., et al., 2014, ApJ, 789, 8
Noble J. A., Dulieu F., Congiu E., Fraser H. J., 2011, ApJ, 735, 121
Podio L., Lefloch B., Ceccarelli C., Codella C., Bachiller R., 2014, A&A, 565, A64
Rivilla V. M., Fontani F., Beltrán M. T., Vasyunin A., Caselli P., Martín-Pintado J., Cesaroni R., 2016, ApJ, 826, 161
Sakai N., Sakai T., Aikawa Y., Yamamoto S., 2008, ApJ, 675, L89
Thaddeus P., Guelin M., Linke R. A., 1981, ApJ, 246, L41
Turner B. E., Terzieva R., Herbst E., 1999, ApJ, 518, 699
van Dishoeck E. F., et al., 1996, A&A, 315, L349
Vastel C., Ceccarelli C., Lefloch B., Bachiller R., 2016, A&A, 591, L2
Vasyunin A. I., Caselli P., Dulieu F., Jiménez-Serra I., 2017, ApJ, 842, 33
Whittet D. C. B., Cook A. M., Chiar J. E., Pendleton Y. J., Shenoy S. S., Gerakines P. A., 2009, ApJ, 695, 94
Öberg K. I., Boogert A. C. A., Pontoppidan K. M., van den Broek S., van Dishoeck E. F., Bottinelli S., Blake G. A., Evans N. J. II, 2011, ApJ, 740, 109

This paper has been typeset from a TEX/LATEX file prepared by the author.